



CHORUS

This is the accepted manuscript made available via CHORUS. The article has been published as:

Origin of the Resistive Anisotropy in the Electronic Nematic Phase of $\text{BaFe}_{2}\text{As}_{2}$ Revealed by Optical Spectroscopy

C. Mirri, A. Dusza, S. Bastelberger, M. Chinotti, L. Degiorgi, J.-H. Chu, H.-H. Kuo, and I. R. Fisher

Phys. Rev. Lett. **115**, 107001 — Published 1 September 2015

DOI: [10.1103/PhysRevLett.115.107001](https://doi.org/10.1103/PhysRevLett.115.107001)

Origin of the resistive anisotropy in the electronic nematic phase of BaFe_2As_2 revealed by optical spectroscopy

C. Mirri*, A. Dusza, S. Bastelberger, M. Chinotti, and L. Degiorgi*
Laboratorium für Festkörperphysik, ETH - Zürich, 8093 Zürich, Switzerland

J.-H. Chu, H.-H. Kuo, and I.R. Fisher
*Geballe Laboratory for Advanced Materials and Department of Applied Physics,
Stanford University, Stanford CA 94305, USA and
Stanford Institute for Materials and Energy Sciences,
SLAC National Accelerator Laboratory, 2575 Sand Hill Road, Menlo Park CA 94025, USA*
(Dated: August 19, 2015)

We perform, as a function of uniaxial stress, an optical-reflectivity investigation of the representative 'parent' ferropnictide BaFe_2As_2 in a broad spectral range, across the tetragonal-to-orthorhombic phase transition and the onset of the long-range antiferromagnetic order (AFM). The infrared response reveals that the *dc* transport anisotropy in the orthorhombic AFM state is determined by the interplay between the Drude spectral weight and the scattering rate, but that the dominant effect is clearly associated with the metallic spectral weight. In the paramagnetic tetragonal phase, though, the *dc* resistivity anisotropy of strained samples is almost exclusively due to stress-induced changes in the Drude weight rather than in the scattering rate, definitively establishing the anisotropy of the Fermi surface parameters as the primary effect driving the *dc* transport properties in the electronic nematic state.

PACS numbers: 74.70.Xa, 78.20.-e

Underdoped compositions of the ferropnictide superconductors exhibit a tetragonal-to-orthorhombic structural phase transition at T_s that either precedes or accompanies the onset of long-range antiferromagnetic (AFM) order at T_N . One of the primary measurements that has led to an understanding of the structural phase transition in terms of electronic nematic order has been the in-plane *dc* resistivity anisotropy [1–4]. In the orthorhombic phase this quantity suggests a substantial electronic anisotropy, while in the tetragonal phase differential elastoresistance measurements (i.e., measurements of the induced resistivity anisotropy due to anisotropic strain) reveal the diverging nematic susceptibility associated with the thermally driven nematic phase transition [5, 6].

There is, however, an ongoing debate as to whether the *dc* anisotropy (both in the nematic phase ($T_N < T < T_s$) or in the tetragonal phase above T_s in the presence of an external symmetry breaking field) is primarily determined by the Fermi surface (FS) or scattering rate anisotropy [6–11]. Recent elastoresistivity experiments have shown that the strain-induced resistivity anisotropy in the tetragonal state of representative underdoped Fe-arsenide families is independent of disorder over a wide range of defect and impurity concentrations and consequently is not due to elastic scattering from anisotropic defects [6, 7]. Nonetheless, measurements of annealed crystals of $\text{Ba}(\text{Fe}_{1-x}\text{Co}_x)_2\text{As}_2$ held under constant yet unknown uniaxial stress indicate that the resistivity anisotropy diminishes after annealing, and therefore suggest that elastic scattering might be significant in determining the resistivity anisotropy in the AFM state [8, 9]. Furthermore, STM measurements [10, 11] at very low

temperatures reveal extended anisotropic defects (i.e., nematogens), perhaps associated with impurities which locally polarize the electronic structure. Both of these observations indicate that the resistivity anisotropy might alternatively be associated with anisotropic elastic scattering from nematogens. Theoretical arguments have been made supporting this perspective [12], but it is far from clear how relevant the suggested mechanism is for the actual material.

In order to clarify the microscopic origin of the resistivity anisotropy in the electronic nematic phase, more thorough experimental studies targeting the impact of the Fermi surface and the quasiparticle scattering rates are desired for temperatures below T_s . Unfortunately, such a study is hampered by twin domain formation below T_s [4, 13] and also by Fermi surface reconstruction in the AFM state. However, measurement of strain-induced optical anisotropy in the high-temperature tetragonal phase (i.e., for $T > T_s$) can directly address the same questions, circumventing both practical concerns. The microscopic mechanisms that result in the electronic anisotropy in the paramagnetic orthorhombic phase (i.e., the nematic phase) are the same as those in the strained tetragonal phase [3, 6, 7]. In other words, measurements of the anisotropy of the optical conductivity for strained samples in the tetragonal phase directly connects to the electronic nematicity, and yet, of particular importance, is not affected by either FS reconstruction or twin boundary motion (since the material is homogeneous in the tetragonal phase).

Here, we address the controversial debate on the *dc* anisotropy via measurements of the optical reflectivity ($R(\omega)$) of the representative 'parent' compound

BaFe₂As₂, across the structural transition and upon tuning *in-situ* the symmetry-breaking field represented by in-plane uniaxial compressive stress. The $R(\omega)$ measurement is an excellent probe in order to study the impact of the nematic phase in the orthorhombic state and its fluctuations in the tetragonal phase on the charge dynamics and electronic properties, since (unlike *dc* measurements) it spans a vast energy interval, extending from the FS to energies deep into the electronic structure. From $R(\omega)$ we determine the real part $\sigma_1(\omega)$ of the optical conductivity, from which we unambiguously extract the Drude weight and scattering rate in the two crystallographic directions. Our main result is that the *dc* resistivity anisotropy is dominated by anisotropy in the spectral weight rather than in the scattering rate. In the long-range AFM state, both the scattering rate and spectral weight anisotropy contribute to the *dc* resistivity anisotropy, but the spectral weight is the dominant effect. However, in the tetragonal phase the strain-induced elasto-resistance anisotropy is almost completely determined by the spectral weight anisotropy. This result definitively establishes that the primary effect driving the resistivity anisotropy in the paramagnetic orthorhombic state (i.e., the electronic nematic phase) is the anisotropy of the FS parameters (i.e., anisotropy in the Fermi velocity v_F , effective mass m^* and/or Fermi wave-vector k_F under an in-plane rotation of 90 degrees).

The BaFe₂As₂ single crystal for this study was grown using a self-flux method, as described previously [14]. The structural and magnetic transition occur at $T_s \sim T_N = 135$ K (from now on denoted as $T_{s,N}$). In order to overcome the formation of dense structural twins below $T_{s,N}$ [4, 13], which mask the anticipated in-plane optical anisotropy, we recently developed a technique using a spring bellows to tune the uniaxial compressive stress that is exerted on samples in order to detwin them [15, 16]. The applied uniaxial stress is quantified by the pressure (p) of He-gas, flushed inside the bellows in order to control its expansion. Further details about the experimental technique and setup can be found in Refs. 15 and 16 as well as in Supplemental Material [17]. The in-plane $R(\omega)$ was measured from the far infrared (FIR) to the ultraviolet (UV) at nearly normal incidence [18] with the electromagnetic radiation polarized along the orthorhombic antiferromagnetic a and ferromagnetic b axes. Data were collected in the energy interval $\omega \sim 60$ to 7000 cm⁻¹, following an initial 'zero-pressure-cool' (ZPC) [15]. Such a protocol is reminiscent of the zero-field-cooling procedure for magnetization measurements in a ferromagnet: from above $T_{s,N}$ we cool down the sample to the selected temperature (T), without applying any pressure. At that T , kept fixed during the whole experiment, we progressively increase p in steps of 0.2 bar from 0 to a maximum pressure of 0.8 bar and measure $R(\omega)$ at each step. Then, we complete the 'pressure loop' by measuring $R(\omega)$ when releasing p back to 0 bar. The sample was thermalized at $T \gg T_{s,N}$ before performing a ZPC for the next measurement at a different tempera-

ture. These data were complemented with measurements up to 40000 cm⁻¹ on unstressed sample at 300 K. The optical conductivity was then extracted from the $R(\omega)$ spectrum by Kramers-Kronig (KK) transformations [18].

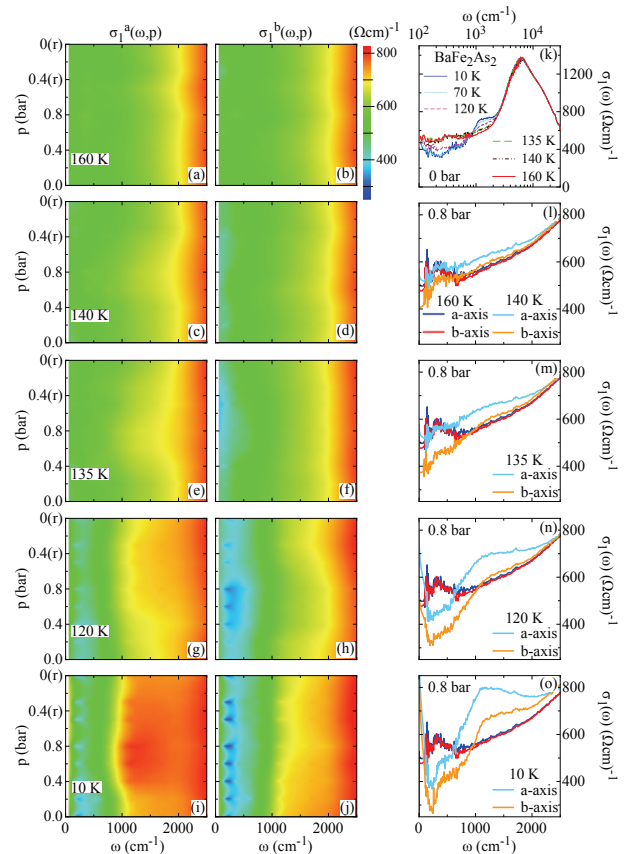


FIG. 1: (color online) The color maps display the pressure dependence of the real part $\sigma_1(\omega)$ of the optical conductivity up to 2500 cm⁻¹ along the a and b axis at selected temperatures: (a,b) 160 K, (c,d) 140 K, (e,f) 135 K, (g,h) 120 and (i,l) 10 K. Data have been interpolated using a first-neighbor interpolation procedure to generate the color maps. Released pressures are denoted by 'r'. The upper right panel (m) shows the temperature dependence of $\sigma_1(\omega)$ in the FIR-UV range at 0 bar (i.e., twinned sample). The in-plane optical conductivity of BaFe₂As₂ at $p = 0.8$ bar, compared to the data at 160 K at the same p , is also shown up to 2500 cm⁻¹ at the selected temperatures: (n) 140 K, (o) 135 K, (p) 120 K, and (q) 10 K.

Figure 1 displays the real part $\sigma_1(\omega)$ of the optical conductivity. The upper right panel (m) (in a semi-log scale) emphasizes the temperature dependence of $\sigma_1(\omega)$ for the unstressed (twinned) specimen, in overall good agreement with our previous results [19]. At $T \geq T_{s,N}$, $\sigma_1(\omega)$ is weakly temperature dependent, tending to a constant value in the FIR range, as is common for a conducting material. Below $T_{s,N}$, the transition into the long-range AFM state opens a partial gap, which depletes $\sigma_1(\omega)$ in FIR below 1000 cm⁻¹ and, due to the reshuffled spectral weight, leads to an enhancement at

mid-infrared (MIR) frequencies, forming a peak centered at about 1300 cm^{-1} . The un-gapped portion of the FS contributes to the metallic response of $\sigma_1(\omega)$ finally merging into a narrow zero-energy mode below 200 cm^{-1} . The temperature dependence of $\sigma_1(\omega)$ expires above 3000 cm^{-1} at the onset of the near-infrared (NIR) absorption peaked around 7000 cm^{-1} and attributed to electronic interband transitions [20, 21].

The color maps of Fig. 1 reproduce the p dependence of $\sigma_1(\omega)$ in the FIR-MIR spectral range ($\omega \sim 60 - 2500 \text{ cm}^{-1}$) at selected temperatures above, at and below $T_{s,N}$. The lower the temperature, the stronger is the optical anisotropy achieved upon applying uniaxial stress. Along the a axis, the depletion in FIR becomes less pronounced, the intensity of the MIR absorption increases and its peak frequency shifts to lower energy upon increasing p . Quite the opposite behavior is observed along the b axis (see e.g. Fig. 1(i,l)). The resulting optical anisotropy saturates at 0.8 bar for $T \ll T_{s,N}$. The right panels (n-q) emphasize the T dependence of the optical response for the single domain specimen (i.e., at saturation for $p = 0.8$ bar), compared with $\sigma_1(\omega)$ at 160 K at the same p . The enhancement of the MIR absorption feature at about 1300 cm^{-1} is clearly evident, primarily along the a axis, as well as the stronger depletion of $\sigma_1(\omega)$ at $\omega < 1000 \text{ cm}^{-1}$ along the b axis with decreasing temperature below $T_{s,N}$. Additionally, we remark the low temperature narrowing of $\sigma_1(\omega)$ at $\omega < 300 \text{ cm}^{-1}$ (Fig. 1(p,q)), which is more pronounced along the b axis. Upon releasing the compressive stress back to zero, a remanent anisotropy still persists at temperatures $T < T_{s,N}$ (Fig. 1(i,l)), but it fully collapses at $T \cong T_{s,N}$ (Fig. 1(e,f)). In other words, we can be certain that the orthorhombic state is strongly anisotropic even in the absence of any external strain. The p -dependent optical anisotropy at $T \leq T_s$ is thus reminiscent of a hysteretic behavior [15, 16], which is consistent with earlier magnetoresistance measurements using an in-plane magnetic field in order to partially detwin single crystal samples [4, 22]. Moreover, the weakly p -dependent stress-induced anisotropy in $\sigma_1(\omega)$ for $T > T_s$ is observable for temperatures up to at least 160 K for $p \geq 0.4$ bar (Fig. 1(c,d,n,e,f,o)) and is reversible upon sweeping p .

In order to analyze our results, we fit the optical response functions by means of the phenomenological Drude-Lorentz model [18]. The fit components for $\sigma_1(\omega)$ are displayed in Fig. 2(g). The free-carrier contribution is described by a broad (B) and a narrow (N) Drude term (Drude $_B$ and Drude $_N$, respectively), mimicking the multiband nature of BaFe_2As_2 . Instead of the simple Drude model that assumes a single band, the normal-state optical properties are best described by a two-Drude model that considers two separate electronic subsystems [23]. The multiband nature of the title compound also precludes the use of the popular generalized-Drude approach commonly applied to single-band materials. At finite frequencies we add three harmonic oscillators (h.o.) FIR, MIR and NIR for the respective spectral

ranges (components (1-3) in Fig. 2(g)) and two high-frequency (VIS-1/2) and temperature-independent h.o.'s (components (4-5) in Fig. 2(g)) covering the energy interval from the visible up to the UV range. We make use of the same set of components at all p and T as well as for both polarization directions, with the exception of the optical-phonon (OP) which appears only along the b axis at $T < T_{s,N}$ [9, 24]. A detailed presentation of the fit procedure and parameters as well as of its components assignment is given in Ref. 17.

For the rest of this letter, we focus our attention on the Drude parameters (Fig. S1 in Ref. 17), which fully determine the dc properties. Panels (a-d) in Fig. 2 display the anisotropy of the plasma frequencies ($\omega_{pN/B}$) and scattering rates ($\Gamma_{N/B}$), given by the ratio of both quantities between the two axes. The anisotropy in the scattering rates ($\Gamma_{N/B}^a/\Gamma_{N/B}^b$) only develops well below $T_{s,N}$ (Fig. 2(a,c)). Indeed, above and across $T_{s,N}$ both Γ_B and Γ_N are fully isotropic. For $T \ll T_{s,N}$ Γ_B is significantly larger (i.e., broadening of the Drude term) and Γ_N tends to weakly decrease (i.e., narrowing of the Drude term) along the a axis with respect to the b axis for the fully detwinned ($p \sim 0.8$ bar) specimen (see also Fig. S1(1,n) in Ref. 17). The anisotropy of the scattering rate Γ_B is consistent with the well-established magnetic order (i.e., enhanced scattering with large momentum transfer along the antiferromagnetic a axis) [4, 25]. The plasma frequency of the narrow Drude term (Fig. 2(d)) is almost fully isotropic and temperature independent (i.e., $\omega_{pN}^a/\omega_{pN}^b \sim 1$). For the broad Drude term (Fig. 2(b)), the more single-domain the sample and the lower T are (see also Fig. S1(i) in Ref. 17), the larger is the plasma frequency along the a axis than along the b axis (i.e., $\omega_{pB}^a/\omega_{pB}^b > 1$). Therefore, it is the broad Drude term that is most strongly affected by the structural and magnetic transition at $T_{s,N}$. The p and T evolution of the Drude weight anisotropy clearly implies an important reshuffling of spectral weight, which for $T < T_{s,N}$ is closely related to the reconstruction of the Fermi surface. While the analysis of the anisotropic spectral weight distribution is left for a forthcoming publication, we remark that along the a axis the spectral weight moves from high towards low frequencies while the opposite trend is observed along the b axis. This reshuffling of spectral weight occurs beyond the FIR h.o. and hence is not an artifact caused by our fitting procedure [17].

We now explicitly turn our attention to the anisotropy of the total Drude weight ($SW_{Drude} = \omega_{pN}^2 + \omega_{pB}^2$), which is shown in Fig. 2(e,f). Contrary to the scattering rates, the anisotropy of the Drude weight (i.e., FS parameters) is strongly enhanced when approaching $T_{s,N}$ from above for finite uniaxial pressure (Fig. 2(f)). This FS related anisotropy grows stronger upon decreasing the temperature below $T_{s,N}$ (Fig. 2(e)). This observation (i.e. that the dominant contribution to the anisotropy of the Drude response for $T \geq T_s$ arises from anisotropy of the spectral weight, and not anisotropy of the scattering rate) is in agreement with conclusions drawn from recent elastore-

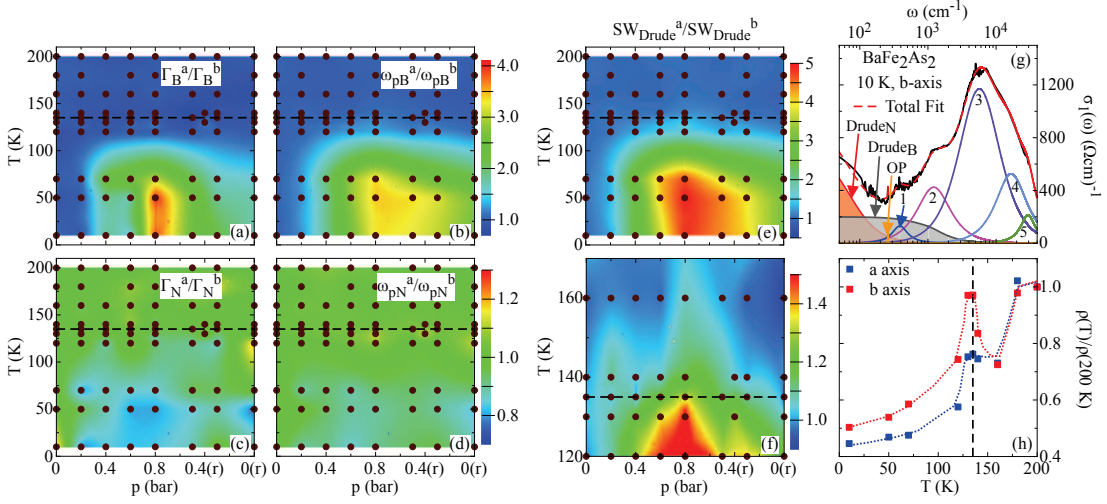


FIG. 2: (color online) (a-d) Pressure and temperature dependence of the anisotropy between the a and b axes (see text) of the plasma frequencies $\omega_{pN/B}$ and the scattering rates $\Gamma_{N/B}$ for the narrow (N) and broad (B) Drude components (Fig. S1 in Ref. 17). (e) Pressure and temperature dependence of the anisotropy ($SW_{Drude}^a/SW_{Drude}^b$) of the total Drude weight ($SW_{Drude} = \omega_{pN}^2 + \omega_{pB}^2$, for both axes). (f) Pressure dependence of the Drude weight anisotropy emphasized at temperatures above 120 K, i.e. close to and above $T_{s,N}$. The dots indicate the fitted (p, T) points, which have been interpolated using a first-neighbor interpolation procedure to generate the color maps. Released pressures are denoted by ‘(r)’. (g) Fit components of the optical conductivity along the b axis in BaFe₂As₂, at 10 K and 0 bar, considered within the Drude-Lorentz approach (Eq. S1 in Ref. 17): Drude _{N/B} , optical phonon (OP), FIR (1), MIR (2), NIR (3), VIS-1 (4) and VIS-2 (5) h.o.’s. Apart from the OP contribution, an equivalent set of fit components is considered along the a axis. (h) The temperature dependence of $\rho(T) = [\sigma_1(\omega = 0, T)]^{-1}$ from the fit of the optical conductivity at 0.8 bar (i.e., at saturation). Each resistivity curve has been normalized at 200 K. The dotted lines in (h) are guide to the eyes. The dashed line in all panels indicates the transition temperature $T_{s,N}$.

sistance measurements [7], but is shown here explicitly. A similar perspective has been advanced based on band structure calculations [26].

We continue our analysis with the calculation of the dc transport properties by reconstructing the dc limit of the optical conductivity $\sigma_1(\omega = 0, T) = \frac{\omega_{pB}^2}{4\pi\Gamma_B} + \frac{\omega_{pN}^2}{4\pi\Gamma_N}$ from the parameters of the two Drude terms. Figure 2(h) displays $\rho(T) = [\sigma_1(\omega = 0, T)]^{-1}$ evinced from the fit of the optical conductivity at 0.8 bar (see also Fig. S6 in Ref. 17 for the complete T and p dependence of ρ), which is in very good agreement with the T dependence of the transport data collected on samples held under a constant uniaxial pressure [1]. In particular, the anisotropy of the dc transport properties can be clearly reproduced for strained samples in the tetragonal regime, for $T > T_{s,N}$, which was first recognized in the transport measurement and which arises from the growing nematic susceptibility associated with the nematic phase transition [5].

Even though the multiband nature of the iron-pnictides hampers precisely tracking the behavior of each single band crossing the Fermi level, our findings reveal a large anisotropy of the resulting conduction bands upon detwinning the specimen. This is reflected in the enhanced metallic (Drude) spectral weight along the a axis with respect to the b axis, which progressively evolves with external stress upon lowering T (Fig. 2(e,f)). From an experimental point of view, it then turns out that

the interplay of both plasma frequency and scattering rate is essential for $T < T_{s,N}$, where the FS is reconstructed, when accounting for the transport properties (Fig. 2(h)). Significantly, though, the anisotropy in scattering rate (Fig. 2(a,c)) on its own would yield a resistivity anisotropy that is opposite to that which is observed, and we therefore conclude that the dominant effect determining the transport anisotropy is in fact associated with changes in the FS parameters (Fig. 2(b,d,e,f)). Similarly, above the structural transition the anisotropy of the Drude weight of stressed samples (Fig. 2(f)) is also primarily responsible for the anisotropic low-frequency optical and dc properties.

Our results put some constraints on future theoretical approaches aimed reproducing the electrodynamic response and its relationship to the dc transport properties of iron-pnictides with respect to their nematic state. Theoretical work has mostly focussed on either anisotropic inelastic scattering with spin fluctuations [12, 27–31] or an anisotropic Drude weight [32, 33]. It remains to be seen how our experimental results and their analysis may be reconciled within theoretical approaches jointly addressing both Drude weight and scattering processes. Even though impurity scattering can affect the transport anisotropy in subtle ways, it seems to have at best only limited relevance in the electronic nematic phase. Furthermore, there is an apparent discrepancy concerning the anisotropy of the experimental Drude scattering

rates and the conclusions drawn from recent theoretical treatments of nematogen scattering [30], which yield opposite trends, and hence appears to not be the dominant effect in shaping the resistivity anisotropy. In order to solve and clarify that discrepancy, a central task would be to figure out which scattering mechanisms dominate in optical experiments. This could indicate possible theoretical avenues in order to shed light on the interplay between scattering rate and Drude weight, as shown by our work.

The authors wish to thank E. Bascones, R. Fernandes, A. Chubukov, P. Hirschfeld, W. Ku, E.W. Carlson, M. Sigrist, S. Kivelson, M. Dressel, D.N. Basov and D. Lu

for fruitful discussions. This work was supported by the Swiss National Science Foundation (SNSF). Work at Stanford University was supported by the Department of Energy, Office of Basic Energy Sciences under contract DE-AC02-76SF00515. L.D. acknowledges the hospitality at KITP (UC Santa Barbara) within the IRONIC14 Workshop, where part of this paper was conceived.

* Correspondence and requests for materials should be addressed to: L. Degiorgi and C. Mirri, Laboratorium für Festkörperphysik, ETH - Zürich, 8093 Zürich, Switzerland; email: degiorgi@solid.phys.ethz.ch, chiara@phys.ethz.ch

-
- [1] J.-H. Chu, J.G. Analytis, K. De Greve, P.L. McMahon, Z. Islam, Y. Yamamoto, and I.R. Fisher, *Science* **329**, 824 (2010).
- [2] E.C. Blomberg, M.A. Tanatar, A. Kreyssig, N. Ni, A. Thaler, Rongwei Hu, S.L. Bud'ko, P.C. Canfield, A.I. Goldman, and R. Prozorov, *Phys. Rev. B* **83**, 134505 (2011).
- [3] E.C. Blomberg, A. Kreyssig, M.A. Tanatar, R.M. Fernandes, M.G. Kim, A. Thaler, J. Schmalian, S.L. Bud'ko, P.C. Canfield, A.I. Goldman, and R. Prozorov, *Phys. Rev. B* **85**, 144509 (2012).
- [4] I.R. Fisher, L. Degiorgi, and Z.X. Shen, *Rep. Prog. Phys.* **74**, 124506 (2011) and references therein.
- [5] J.-H. Chu, H.-H. Kuo, J.G. Analytis, and I.R. Fisher, *Science* **337**, 710 (2012).
- [6] H.-H. Kuo, M.C. Shapiro, S.C. Riggs, and I.R. Fisher, *Phys. Rev. B* **88**, 085113 (2013).
- [7] H.-H. Kuo and I.R. Fisher, *Phys. Rev. Lett.* **112**, 227001 (2014).
- [8] S. Ishida, M. Nakajima, T. Liang, K. Kihou, C.H. Lee, A. Iyo, H. Eisaki, T. Kakeshita, Y. Tomioka, T. Ito, and S. Uchida, *Phys. Rev. Lett.* **110**, 207001 (2013).
- [9] M. Nakajima, S. Ishida, Y. Tomioka, K. Kihou, C.H. Lee, A. Iyo, T. Ito, T. Kakeshita, H. Eisaki, and S. Uchida, *Phys. Rev. Lett.* **109**, 217003 (2012).
- [10] T.-M. Chuang, M.P. Allan, J. Lee, Y. Xie, N. Ni, S.L. Bud'ko, G.S. Boebinger, P.C. Canfield, and J.C. Davis, *Science* **327**, 181 (2010).
- [11] M.P. Allan, T.-M. Chuang, F. Masee, Y. Xie, N. Ni, S.L. Bud'ko, G.S. Boebinger, Q. Wang, D.S. Dessau, P.C. Canfield, M.S. Golden, and J.C. Davis, *Nature Physics* **9**, 220 (2013).
- [12] M.N. Gastiasoro, I. Paul, Y. Wang, P.J. Hirschfeld, and B.M. Andersen, *Phys. Rev. Lett.* **113**, 127001 (2014).
- [13] M.A. Tanatar, A. Kreyssig, S. Nandi, N. Ni, S.L. Bud'ko, P.C. Canfield, A.I. Goldman, and R. Prozorov, *Phys. Rev. B* **79**, 180508(R) (2009).
- [14] J.-H. Chu, J.G. Analytis, C. Kucharczyk, and I.R. Fisher, *Phys. Rev. B* **79**, 014506 (2009).
- [15] C. Mirri, A. Dusza, S. Bastelberger, J.-H. Chu, H.-H. Kuo, I.R. Fisher, and L. Degiorgi, *Phys. Rev. B* **89**, 060501(R) (2014), and Supplemental Material therein.
- [16] C. Mirri, A. Dusza, S. Bastelberger, J.-H. Chu, H.-H. Kuo, I.R. Fisher, and L. Degiorgi, *Phys. Rev. B* **90**, 155125 (2014).
- [17] Supplemental Material at [URL will be inserted by publisher], which provides further details of the sample preparation and experimental technique as well as the fitting procedure. It also includes additional Refs. 34–38.
- [18] M. Dressel and G. Grüner, *Electrodynamics of Solids*, Cambridge University Press, Cambridge, England (2002).
- [19] A. Lucarelli, A. Dusza, F. Pfuner, P. Lerch, J.G. Analytis, J.-H. Chu, I.R. Fisher, and L. Degiorgi, *New. J. Phys.* **12**, 073036 (2010).
- [20] A. Sanna, F. Bernardini, G. Profeta, S. Sharma, J.K. Dewhurst, A. Lucarelli, L. Degiorgi, E.K.U. Gross, and S. Massidda, *Phys. Rev. B* **83**, 054502 (2011).
- [21] Z.P. Yin, K. Haule, and G. Kotliar, *Nature Physics* **7**, 294 (2011).
- [22] J.-H. Chu, J.G. Analytis, D. Press, K. De Greve, T.D. Ladd, Y. Yamamoto, and I.R. Fisher, *Phys. Rev. B* **81**, 214502 (2010).
- [23] D. Wu, N. Barišić, P. Kallina, A. Faridian, B. Gorshunov, N. Drichko, L.J. Li, X. Lin, G.H. Cao, Z.A. Xu, N.L. Wang, and M. Dressel, *Phys. Rev. B* **81**, 100512(R) (2010).
- [24] A.A. Schafgans, B.C. Pursley, A.D. LaForge, A.S. Sefat, D. Mandrus, and D.N. Basov, *Phys. Rev. B* **84**, 052501 (2011).
- [25] A. Dusza, A. Lucarelli, A. Sanna, S. Massidda, J.-H. Chu, I.R. Fisher, and L. Degiorgi, *New. J. Phys.* **14**, 023020 (2012).
- [26] M.A. Tanatar, E.C. Blomberg, A. Kreyssig, M.G. Kim, N. Ni, A. Thaler, S.L. Bud'ko, P.C. Canfield, A.I. Goldman, I.I. Mazin, and R. Prozorov, *Phys. Rev. B* **81**, 184508 (2010).
- [27] P. Prelovšek, I. Sega, and T. Tohyama, *Phys. Rev. B* **80**, 014517 (2009).
- [28] R.M. Fernandes, E. Abrahams, and J. Schmalian, *Phys. Rev. Lett.* **107**, 217002 (2011).
- [29] M. Breitzkreiz, P.M.R. Brydon, and C. Timm, *Phys. Rev. B* **90**, 121104(R) (2014).
- [30] M.N. Gastiasoro, P.J. Hirschfeld, and B.M. Andersen, *Phys. Rev. B* **89**, 100502(R) (2014).
- [31] Y. Wang, M.N. Gastiasoro, B.M. Andersen, M. Tomić, H.O. Jeschke, R. Valentí, I. Paul, and P.J. Hirschfeld, *Phys. Rev. Lett.* **114**, 097003 (2015).
- [32] S. Liang, G. Alvarez, C. Sen, A. Moreo, and E. Dagotto, *Phys. Rev. Lett.* **109**, 047001 (2012).

- [33] B. Valenzuela, E. Bascones, and M.J. Calderón, Phys. Rev. Lett. **105**, 207202 (2010).
- [34] L. Benfatto, E. Cappelluti, L. Ortenzi, and L. Boeri, Phys. Rev. B **83**, 224514 (2011).
- [35] B. Valenzuela, M. J. Calderón, G. León, and E. Bascones, Phys. Rev. B **87**, 075136 (2013).
- [36] M. J. Calderón, L. de'Medici, B. Valenzuela, and E. Bascones, Phys. Rev. B **90**, 115128 (2014).
- [37] A.A. Schafgans, S.J. Moon, B.C. Pursley, A.D. LaForge, M.M. Qazilbash, A.S. Sefat, D. Mandrus, K. Haule, G. Kotliar, and D.N. Basov, Phys. Rev. Lett. **108**, 147002 (2012).
- [38] Q. Si, Nature Physics **5**, 629 (2009).